# Satellite evidence for China's leading role in restoring vegetation productivity over global karst ecosystems

Xuguang Tang[a,b,*], Jingfeng Xiao[c], Mingguo Ma[a,b,*], Hong Yang[d], Xing Li[c], Zhi Ding[a,b], Pujia Yu[a,b], Yongguang Zhang[e], Chaoyang Wu[f], Jing Huang[a,b], Julian R. Thompson[g]

[a] Chongqing Jinfo Mountain Karst Ecosystem National Observation and Research Station, School of Geographical Sciences, Southwest University, Chongqing 400715, China.

[b] Chongqing Engineering Research Center for Remote Sensing Big Data Application, Southwest University, Chongqing 400715, China.

[c] Earth Systems Research Center, Institute for the Study of Earth, Oceans, and Space, University of New Hampshire, Durham, NH 03824, USA.

[d] Department of Geography and Environmental Science, University of Reading, Whiteknights, Reading RG6 6AB, UK.

[e] International Institute for Earth System Sciences, Nanjing University, Nanjing 210023, China.

[f] The Key Laboratory of Land Surface Pattern and Simulation, Institute of Geographical Sciences and Natural Resources Research, Chinese Academy of Sciences, Beijing 100101, China.

[g] Department of Geography, University College London, London WC1E 6BT, UK.

Corresponding authors: X. T. (email: xgtang@swu.edu.cn), M.M. (email: mmg@swu.edu.cn).

**Abstract**: Karst ecosystems occupy approximately 20% of the Earth's land surface with the unique and vulnerable geomorphological and hydrogeological characteristics. To date, it remains a challenge to accurately monitor ecosystem productivity from space, as well as their responses to the environmental conditions due to climate change and anthropogenic pressure, which is pivotal to the sustainable development strategies in global karst areas. Here we use a reconstructed long-term solar-induced chlorophyll fluorescence dataset (SIF) and two satellite-based gross primary productivity (GPP) products to examine the patterns and trends of vegetation productivity within global karst ecosystems, and to assess the relative contributions of different countries to the restoration of these fragile ecosystems over the period 2001–2016. As an effective proxy for terrestrial GPP, SIF reveals a greening trend across most of the world's karst areas. China and the European Union (EU) lead the world in vegetation greening within their karst areas by 78.02% and 42.44%, respectively. The total net increase in SIF shows that China alone accounted for 43.66% with just 7.0% of global karst area. Brazil is the only country with a negative greening trend. Recent land cover changes caused by the grain-for-green programme in China and deforestation in Brazil account for 36.93% and 64.71% of the increases and decreases, respectively. Our results have significant implications for restoring ecosystem productivity in global karst areas.

**Keywords:** Karst ecosystem; Vegetation restoration; Solar-induced chlorophyll fluorescence; GPP; LUCC

## 1. Introduction

Global environmental change has rapidly altered terrestrial vegetation, with consequent impacts on the functioning of the Earth system and the provision of ecosystem services (Grimm *et al*., 2013). Long-term changes in vegetation can be attributed to multiple interacting factors including changes in climate and anthropogenic activities, particularly land use and land cover changes (Piao *et al*., 2015; Mao *et al*., 2016; Keenan *et al*., 2018). Despite the observed greening of many parts of the globe derived from a range of satellite data over the last decade (Ju & Masek, 2016; Zhu *et al*., 2016), uncertainties still remain regarding the dominant controls of the trends, the spatial differences, and the possibility of continued greening in face of future environmental change. In particular, the responses of the world's ecologically-fragile areas, including karst ecosystems, to the changing environmental conditions are not well understood.

Karst landscapes, characterized by features such as caves, sinkholes and extensive underground water flow systems developed on predominantky limestone geologies, link the Earth's surface to the subsurface (De Waele *et al*., 2015). Approximately 25% of the world population depends upon natural resources and ecosystem services derived from karst ecosystems (Ford & Williams, 2013). Given the large extent and wide distribution of karst terrain around the world (Fig. S1), these ecosystems play important roles in regulating the terrestrial carbon cycle and potentially mitigating climate change. However, rocky desertification has emerged as one of the most serious environmental problems in karstic areas because of long-term overexploitation. It is a process of land degradation involving serious soil erosion, extensive exposure of underlying rocks,

drastic declines in soil productivity, and the appearance of a desert-like landscape. The occurrence and magnitude of these environmental changes vary around the world. Of the three largest global karst regions, the eastern North America and middle and southern parts of Europe are relatively unaffected. In contrast, the large karst area of East Asia has seen widespread rocky desertification and is now recognized as an ecologically-fragile region (Yan & Zhong, 2011). Appropriate management strategies to prevent and control the expansion of rocky desertification are critically necessary for the sustainable development of global karst ecosystems. Several counties including China have implemented large-area ecological conservation projects to combat desertification and improve ecological conditions (Laffoon *et al*., 2014; Tong *et al*., 2018). Long-term management of such initiatives requires accurate monitoring of restoration progress.

Several different approaches have been used to monitor the variability in terrestrial gross primary productivity (GPP) including satellite-derived vegetation indices, light-use efficiency models and process-based models (Piao *et al*., 2015; Zhu *et al*., 2016; Wu *et al*., 2018). However, these methods are often associated with large discrepancies due to uncertainties in model algorithm or input data (Guanter *et al*., 2014). Alternatively, satellite observations of solar-induced chlorophyll fluorescence (SIF), particularly from the Orbiting Carbon Observatory-2 (OCO-2) mission, provide a novel proxy for GPP across multiple spatiotemporal scales. These data are valuable for studying ecosystem dynamics and carbon–climate feedbacks (Walther *et al*., 2016; Sun *et al*., 2017). However, the spatially and temporally sparse SIF retrievals for OCO-2 constrain their applications from regional to global scales. The development of a global spatially

contiguous SIF dataset with finer resolution offers the possibility of accurately and repeatedly monitoring terrestrial photosynthesis and ecosystem productivity at various spatiotemporal scales (Zhang *et al*., 2018; Li & Xiao, 2019). Here, we use a new globally, reconstructed OCO-2 based SIF dataset (GOSIF) from 2001 to 2016, together with two widely-used satellite-based GPP products, to (1) analyze the spatial patterns and trends in productivity of the world's karst ecosystems; (2) investigate the progress of different countries in restoring these fragile ecosystems; and (3) assess the prominent environmental controls on the observed trends that include both climatic factors and land cover change. Fig. S2 briefly described the framework of this study.

## 2. Methods and Materials

### *2.1. Global OCO-2 based SIF dataset*

The advent of satellite-derived SIF data promises a new era in monitoring terrestrial ecosystems. Recent studies have confirmed that SIF retrieval from the Orbiting Carbon Observatory-2 (OCO-2) provide a powerful proxy for terrestrial GPP at multiple spatiotemporal scales (Sun *et al*., 2017; Li *et al*., 2018). However, the spatially and temporally sparse nature of OCO-2 data makes it challenging for the applications from the ecosystem level to the globe. Thus, we used a new global, 0.05° SIF data set (GOSIF) at an 8-day interval derived from OCO-2, MODIS and MERRA-2 data (Li & Xiao, 2019). These SIF estimates were found to be significantly correlated with GPP data from 91 FLUXNET sites ($R^2 = 0.73$, $p < 0.001$). Compared with the coarse-resolution SIF data directly aggregated from discrete OCO-2 soundings, GOSIF has the advantages of

finer spatial resolution, globally continuous coverage and a much longer period. It is thus effective for assessing terrestrial photosynthesis and ecosystem function. More details of the methodology, validation, and spatiotemporal characteristics of this product can be found in the reference (Li & Xiao, 2019). In this study, we used the time-series GOSIF dataset from 2001 to 2016 (http://data.globalecology.unh.edu/data/GOSIF_v2/) to analyze long-term vegetation changes in global karst ecosystems. The annual mean SIF for each grid cell was derived from all the 8-day values within each year. Multi-year SIF averages were compared with MODIS and VPM GPP products.

### *2.2. Site-level observations of SIF*

Despite that the satellite-based GOSIF dataset has emerged as a novel and powerful approach for terrestrial vegetation monitoring, its robustness needs to be validated for large-scale applications. Fortunately, several ground-based spectrometer systems have been developed and installed at the eddy covariance (EC) towers in recent years, which provide continuous SIF observations (Magney *et al*., 2019). In total of four tower sites including one subtropical evergreen forest (CN-HT), one subalpine conifer forest (US-NR) and two temperate cropland were used in this study with available high-frequency SIF retrievals since 2017. The details of instrument specifications, data collection and processing procedures can be found in the literature (Zhang *et al*., 2021). As shown in Fig. S3, satellite-based SIF generally agreed well with ground-based SIF measurements over a variety of vegetation types. The coefficient of determination ($R^2$) and root mean square error (RMSE) varied across different sites, with $R^2$ ranging from the minimal of 0.688 at CN-HT to the maximal of 0.874 at US-NR and RMSE ranging from the

maximal of 0.084 W $m^{-2}$ $\mu m^{-1}$ $sr^{-1}$ at CN-DM to the minimal of 0.020 W $m^{-2}$ $\mu m^{-1}$ $sr^{-1}$ at US-NR. Considering that there are still mismatch of the footprint between satellite and ground-based measurements, such direct comparison demonstrated the potential of global OCO-2 based SIF dataset.

### *2.3. MODIS GPP product*

The MOD17A2 GPP product is the first operational satellite-driven dataset to repeatedly monitor global vegetation productivity at 1-km resolution and an 8-day interval (Zhao *et al*., 2005). The dataset is widely used for natural resource and land management, global carbon cycle research, ecosystem status assessment, and environmental change monitoring (Tang *et al*., 2014). The MOD17 algorithm is based on the light use efficiency (LUE) model that relates vegetation photosynthesis to the amount of photosynthetically active radiation (PAR) absorbed by plants during the growth period. The old MODIS GPP product (C4) was revealed to have considerable uncertainties owing to problems in the data inputs. Zhao *et al*. (2005) rectified these products by optimizing the data processing methods and modifying key parameters, thereby generating improved GPP estimates (C5.5). The 8-day composite 1-km fraction of photosynthetically active radiation (FPAR) and leaf area index (LAI) data from the MOD15 product were used as the remotely-sensed vegetation property dynamic inputs to the algorithm. Data gaps in the MODIS LAI/FPAR caused by cloud cover were filled with information from accompanying quality-assessment flags. For the daily meteorological dataset required to drive the algorithm, the 6-h National Center for Environmental Prediction/Department of Energy (NCEP/DOE) reanalysis II data were

147 employed. The associated Biome Parameter Lookup Table (BPLUT) was also updated
148 for different vegetation types. These GPP products over the period 2001–2015 at 8-day,
149 monthly, and annual time steps are currently available from the Numerical
150 Terradynamic Simulation Group (NTSG) of the University of Montana
151 (http://www.ntsg.umt.edu/project/mod17).

152 *2.4. VPM GPP product*

153 The Vegetation Photosynthesis Model (VPM) GPP product (V20) is based on an
154 improved LUE model driven by satellite remote sensing data from MODIS and climate
155 data from NCEP Reanalysis II dataset (Zhang *et al*., 2017). The two main input data
156 comprising the enhanced vegetation index (EVI) and land surface water index (LSWI)
157 in the VPM model were derived from the MOD09A1 (C6) land surface reflectance data
158 with a spatial resolution of 500 m and an 8-day time interval. In addition, the VPM GPP
159 product employed a state-of-the-art vegetation index gap-filling and smoothing
160 algorithm and considered the $C_3$/$C_4$ difference in plant photosynthesis pathways, which
161 solved several critical problems in the main GPP products such as the widely-used
162 MOD17A2. The GPP of each pixel was calculated by area-weighted averaged GPP,
163 which was derived from area fraction maps of $C_3$/$C_4$ plants and land use datasets
164 (MCD12Q1). Across 25 eddy covariance flux tower sites, the VPM GPP estimates
165 showed better accuracy in terms of cross-site variability and interannual variability
166 compared to MOD17 GPP (Wu *et al*., 2018). In this study, the global VPM GPP products
167 between 2001 and 2016 were used for the auxiliary analysis with a spatial resolution of
168 0.05°×0.05°. These 8-day, monthly and annual data can be downloaded freely from the

website https://doi.org/10.6084/m9.figshare.c.3789814.

*2.5. Temperature and precipitation data*

The Global Land Data Assimilation System (GLDAS) combines satellite and ground-based observations, using advanced surface modeling and data assimilation techniques, in order to generate optimal fields of land surface states and fluxes (Hiroko & Rodell, 2016). At present, GLDAS drives four land surface models (LSM): Noah, Catchment, the Community Land Model (CLM) and the Variable Infiltration Capacity (VIC). GLDAS version 2 has two components: one forced entirely with the Princeton meteorological forcing data (GLDAS-2.0) and the other forced with a combination of model and observation-based datasets (GLDAS-2.1). This study used the Noah LSM-based GLDAS-2.1 data at 0.25° resolution from 2001 to 2016 to reveal the dominant factors influencing the long-term trends in annual mean SIF across global karst ecosystems. The monthly meteorological data are generated through temporal averaging of the 3-h products and can be downloaded via http://disc.sci.gsfc.nasa.gov/uui/datasets?keywords=GLDAS. Then, the temperate and precipitation data were synthesized into yearly products (mean annual temperature and annual total precipitation).

*2.6. CCI Land Cover data*

A new time series of consistent global land cover data at 300 m spatial resolution from 1992 to 2015 is provided by the European Space Agency known as the Climate Change Initiative Land Cover (CCI-LC) products (V2). These annual products are

made available through the following website: http://maps.elie.ucl.ac.be/CCI/viewer/download.php. The CCI-LC product used the land cover classification system developed by the United Nations (UN) Food and Agriculture Organization (FAO), with a view of being compatible with the plant functional types used in climate models (Poulter *et al*., 2015). Several studies have demonstrated that CCI-LC products have the largest overall accuracy when compared with another five global land cover datasets including IGBP DISCover, UMD, GLC, MCD12Q1 and GLCNMO (Yang *et al*., 2017). This study analyzed the time-series CCI-LC products from 2001 to 2015 to explore the effect of land cover changes on global karst ecosystem productivity. The land cover classes are grouped into nine IPCC land categories (cropland, forest, grassland, shrubland, sparse vegetation, wetland, settlement, bare area and water) for research purpose.

### *2.7. Trend analysis in global SIF*

The long-term trends of annual mean SIF across terrestrial ecosystems in the karst areas were analyzed through the non-parametric Mann-Kendall (M-K) test (Gocic & Trajkovic, 2013). The M-K method provides the possibility of testing for non-linear development in SIF consistently increasing or decreasing, and does not assume a specific distribution for the time-series data and is insensitive to outliers. Because of these advantages, it has been widely used for trend analysis recently (Fensholt *et al*., 2012). The Theil-Sen method was then used to quantify the magnitude of changes over time. This study assessed the frequency distribution of the trends derived from each pixel in accordance to the significance level ($p$-value) of the change (with $p<0.01$, $p<0.05$ and

212 $p$>0.05 indicating that the increasing or decreasing trends are very significant, significant
213 and insignificant, respectively). The proportions of the karst areas in the top ten
214 countries/region showing significant greening or browning were also evaluated.

215 *2.8. Contribution rates*

216 Using the results of the trend analysis for annual average SIF across global karst
217 areas over the period 2001–2016, the contributions to the restoration of karst
218 ecosystems by countries/region were also assessed. The net changes in SIF for a specific
219 area took into account the effects from both statistically significant greening and
220 browning areas, as well as the magnitudes of trends for each pixel. The areas with
221 statistically insignificant trends were set as zero contribution.

222 $$C_j = \frac{\sum_{i=1}^{n} T_{i,j}}{\sum_{j=1}^{m} \sum_{i=1}^{n} T_{i,j}} \quad (1)$$

223 where $C_j$ is the contribution rate of the country $j$; $m$ is the number of countries
224 containing karst ecosystems ($m$=150 here); $n$ is the pixels with a statistically significant
225 trend in the country $j$; and $T_{i,j}$ is the trend of each pixel. This study used percentages
226 to represent the contribution rate of each country to the overall global change.

227 *2.9. Spatial correlation analysis*

228 The correlation and partial correlation coefficients were performed to reveal the
229 environmental controls, including the temperate and precipitation, on the inter-annual
230 dynamics of SIF across global karst areas (Wang *et al*., 2019). The formula of Pearson's
231 correlation coefficient (r) was as follows:

$$r_{xy} = \frac{\sum_{i=1}^{n}(x_i - \bar{x})(y_i - \bar{y})}{\sqrt{\sum_{i=1}^{n}(x_i - \bar{x})^2}\sqrt{\sum_{n=1}^{n}(y_i - \bar{y})^2}} \quad (2)$$

where $n$ is the length of the time series data; $i$ is the number of year, i=1, 2,…16; and $x_i$ ($y_i$) and $\bar{x}$ ($\bar{y}$) are the values of the $i$ year and the averages of these years, respectively.

The partial correlation coefficient ($r_{yz \cdot x}$) was calculated to reveal the dominant climate factor controlling the variability in SIF. In this way, when assessing the degree of correlations between SIF and temperature (or precipitation), the effect of precipitation (or temperature) is removed:

$$r_{yz \cdot x} = \frac{r_{yz} - r_{yx}r_{zx}}{\sqrt{(1 - r_{yx}^2)(1 - r_{zx}^2)}} \quad (3)$$

where $r_{yz \cdot x}$ represents the partial correlation coefficient between $y$ and $z$ without consideration of the impact of $x$; and $r_{yz}, r_{yx}, r_{zx}$ are the simple correlation coefficients between two variables. Through these analyses, the study identified the dominant environmental controlling factor of each pixel.

# 3. Results

## *3.1. Trends in vegetation dynamics across global karst areas*

The satellite-based SIF data exhibited an overall positive trend for a large proportion of the global karst area since the start of the new millennium (Fig. 1, Fig. S4). The mean annual greening trend was equivalent to 0.0004 W $m^{-2}$ $\mu m^{-1}$ $sr^{-1}$ $yr^{-1}$. Areas with a significant increase in vegetation SIF ($p$<0.05) covered approximately 31.1% of global karst ecosystems, of which one fifth was concentrated in China's southwestern karst area, making China one of the largest, spatially coherent region of vegetation

252 restoration (Fig. S5). The majority (78.02%) of China's karst area experienced
253 significant greening trends, with only less than 1.2% experiencing browning (Table 1).
254 The EU also made a large contribution to the global greening, with 42.44% of its karst
255 area experiencing increasing trends in SIF and only 0.35% showing significant declines.
256 Only a few regions (~2.7% of the global karst area) were identified as having
257 experienced significant negative change over the study period (Fig. S6). Among the top
258 ten countries/region with the largest extent of karst environment (Table 1), Brazil was
259 the only one exhibiting a larger extent of browning (19.43%) than greening (15.83%).

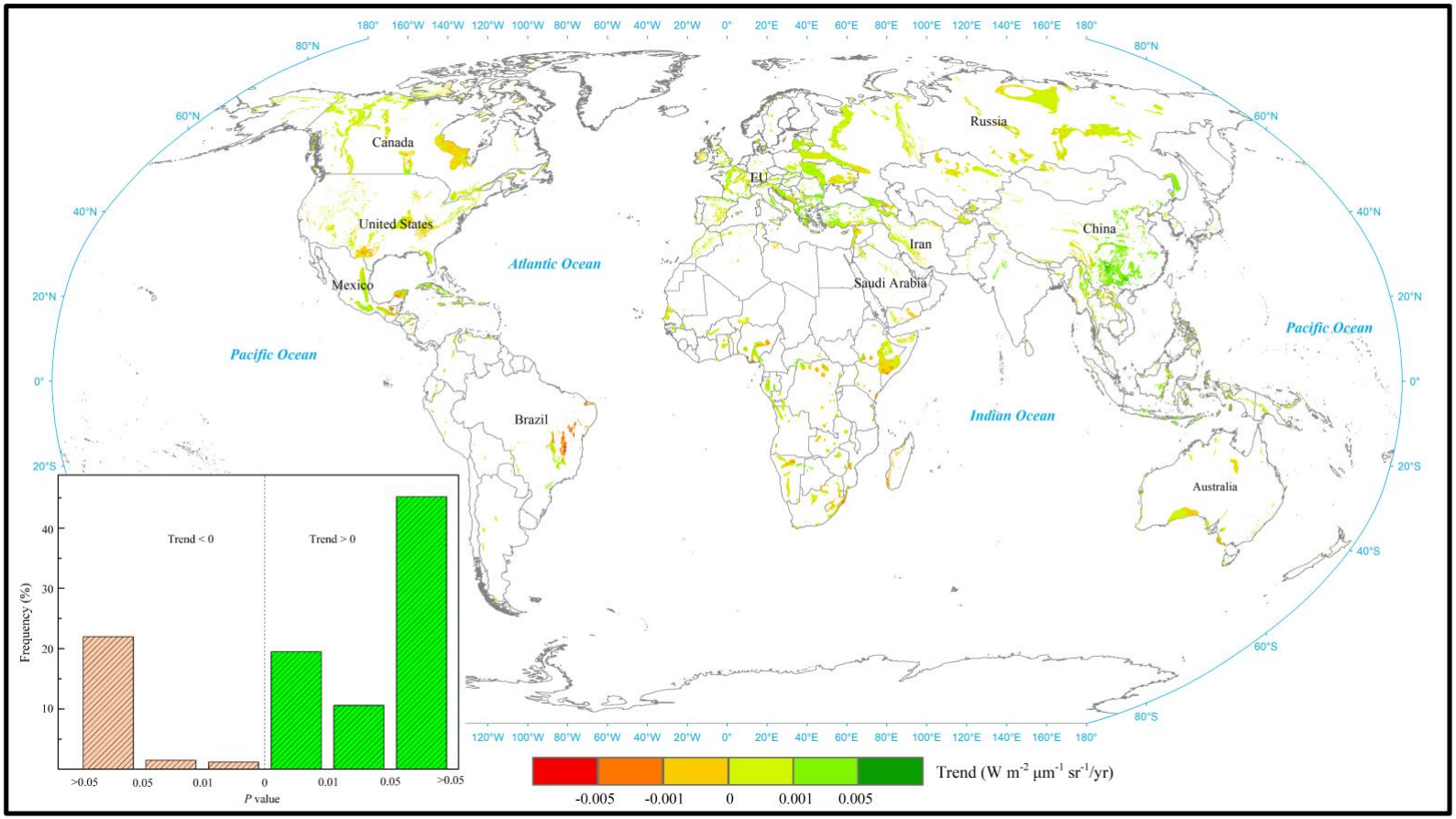


**Fig. 1** Spatial trends of annual mean SIF across global karst ecosystems during the period 2001–2016. The frequency distribution of the significance level (*p*-value) of the trends is derived using the results for all pixels.

263 **Table 1** Vegetation dynamics in the top ten countries/region (EU) with the world's largest karst areas

| Rank | Country | Karst area ($km^2$) | Percentage of total land area | Proportion of areas showing greening | Proportion of areas showing browning | Contribution rate (ranking) |
|---|---|---|---|---|---|---|
| 1 | Russia | 1931825.67 | 11.5% | 25.89% | 2.01% | 11.82% (3) |
| 2 | Canada | 1601205.13 | 16.1% | 29.78% | 2.81% | 6.78% (4) |
| 3 | China | 1121944.83 | 11.9% | 78.02% | 1.14% | 43.66% (1) |
| 4 | United States | 905863.79 | 9.6% | 14.24% | 2.56% | 2.03% (5) |
| 5 | EU | 835650.37 | 19.1% | 42.44% | 0.35% | 11.92% (2) |
| 6 | Saudi Arabia | 612979.41 | 31.9% | 28.00% | 6.98% | 0.22% (9) |
| 7 | Mexico | 606455.46 | 30.9% | 23.03% | 2.26% | 2.00% (6) |
| 8 | Australia | 343070.60 | 4.4% | 8.98% | 1.10% | 0.75% (7) |
| 9 | Brazil | 271195.98 | 3.2% | 15.83% | 19.43% | -1.85% (10) |
| 10 | Iran | 255116.45 | 15.7% | 30.14% | 1.10% | 0.71% (8) |

264 Note: The countries of the European Union (EU) are considered together given the large total karst area and relatively small size of some EU countries. Statistics of
265 the proportion of areas showing greening or browning were significant at 0.05 *p*-level.

Vegetation dynamics in global karst area were also examined by comparing the variations in annual mean SIF and GPP (MODIS and VPM) products from 2001 to 2016 (Fig. 2). The annual global mean SIF had a significant increasing trend of $3.85\times10^{-4}$ W $m^{-2}$ $\mu m^{-1}$ $sr^{-1}$ $yr^{-1}$. Although global mean VPM GPP exhibited a similar positive trend (4.02 g C $m^{-2}$ $yr^{-1}$, $p<0.001$), no significant trend was identified for MODIS GPP ($p>0.05$). Pearson correlation analysis also showed consistency between the SIF dataset and VPM GPP results ($p<0.001$, $r=0.925$) (Fig. S7). Long-term dynamics in the SIF and GPP products over the same period were also evaluated across the top ten countries/region with the largest karst areas (Fig. 3). There were no significant changes for MODIS GPP over all countries, while SIF and VPM GPP generally exhibited similar trends. Despite their large total area, the karst ecosystems in the USA showed no obvious changes in SIF or GPP during the period. In contrast, significant increases were evident for Russia and China. Most notable was the trend in SIF for China's karst vegetation which was nearly five times as large as the global average.

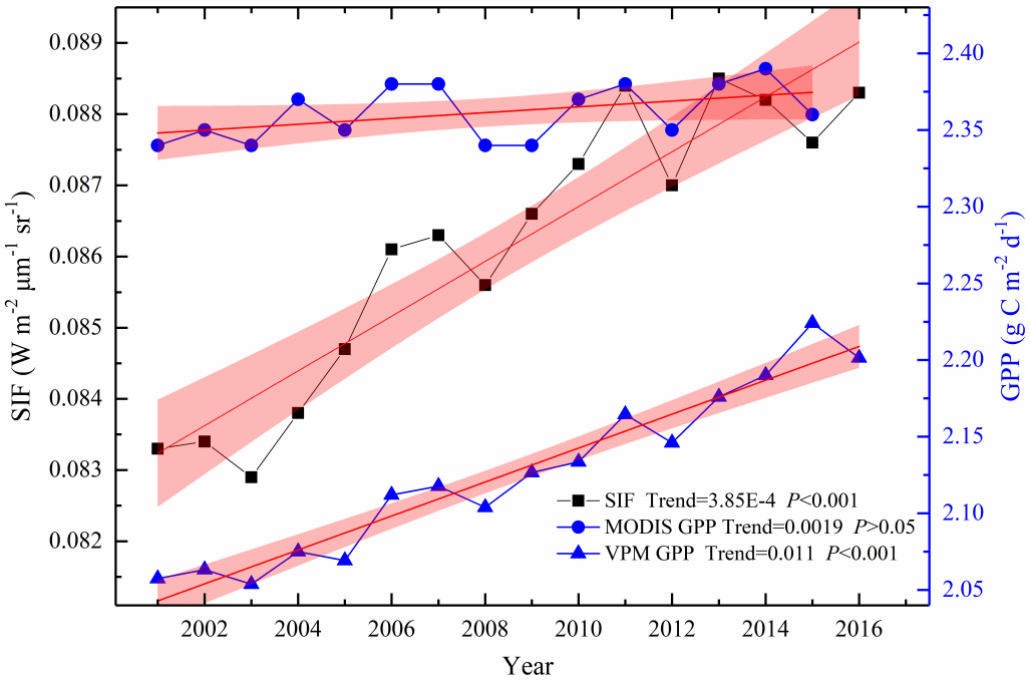


**Fig. 2** Long-term dynamics in SIF and GPP (MODIS and VPM) products across global karst area for the period 2001–2016.

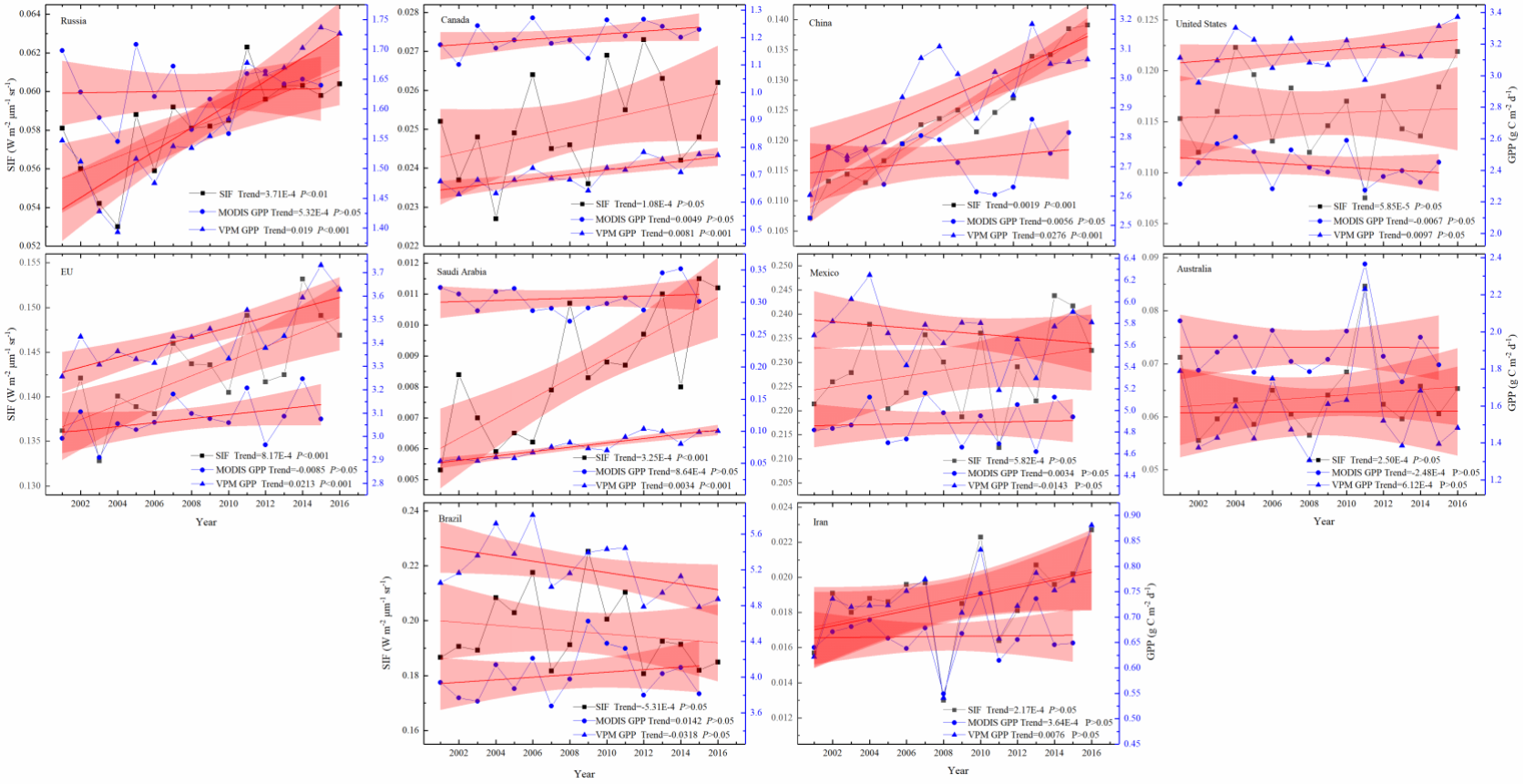


290

291 **Fig. 3** Long-term dynamics in SIF and GPP (MODIS and VPM) products in the top ten countries/region with the largest karst areas around the world during the period

292 2001–2016.

### *3.2. Spatial differences in satellite-observed ecosystem productivity across global karst areas*

As a direct proxy for vegetation photosynthesis, the satellite-based SIF provides a global perspective on terrestrial GPP across the ecologically-fragile karst regions (Fig. 4). In general, the multi-year mean GOSIF data exhibited strong spatial heterogeneity in gross carbon uptake during the period 2001–2016. The largest SIF values appeared primarily in tropical (e.g. Central Africa, Brazil and Mexico) and subtropical (e.g. Southwest China, Southeast USA) regions. Europe's karst ecosystems also exhibited relatively high SIF. In contrast, most karst areas in the mid- and high latitudes exhibited low SIF values (e.g. West Asia, Russia, Canada, western USA and Australia). Comparison of the spatial patterns of multi-year mean MODIS and VPM GPP products over global karst areas (Fig. 5) demonstrated generally good agreement between state-of-the-art satellite data-driven approaches and the SIF observations. Despite similar global patterns, the GPP estimates from MODIS and VPM varied in magnitude. In general, GPP values derived from VPM were larger than those of the MODIS product for karst areas in the eastern USA, Brazil, southwestern China and Europe. In addition, comparison of satellite-based GPP products with SIF retrievals across the top ten countries/region (i.e. the EU) with the largest karst areas (Fig. 6) demonstrated the consistent performance of the different proxies in monitoring spatial patterns in ecosystem productivity. The largest SIF and GPP values are identified in Mexico and Brazil, followed by the EU, China and USA. In contrast, the smallest are found within the karst areas of predominantly arid/semi-arid Iran and Saudi Arabia.

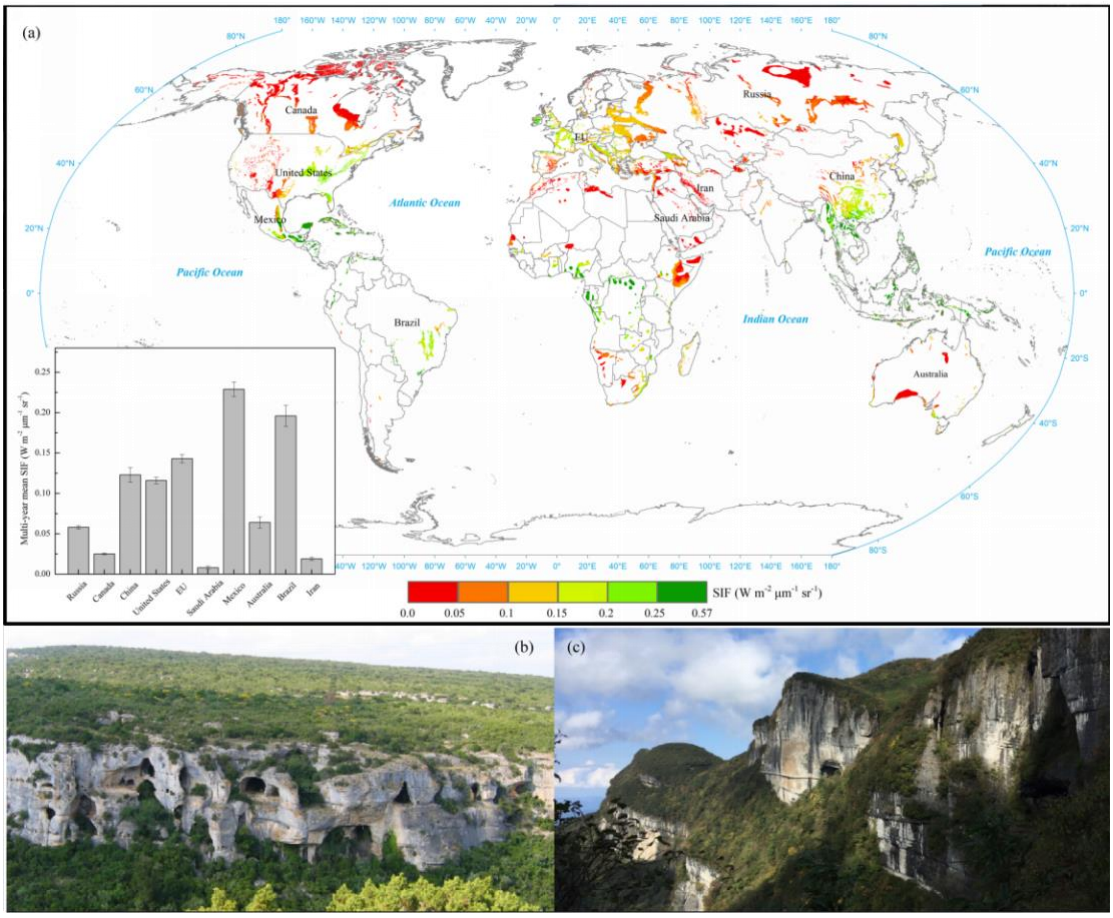


315

316 **Fig. 4** Spatial patterns of multi-year mean SIF across the world's karst areas during the period 2001–
317 2016 (**a**) and typical karst landscapes (**b** and **c**). Multi-year mean SIF in the top ten countries/region
318 (EU) with the largest karst area around the world are indicated. Error bars are ± 1 standard error of
319 the mean. The image (**b**) is Sierra Gorda, Mexico (downloaded from
320 http://upload.wikimedia.org/wikipedia/commons/e/e9/Karst_minerve.jpg.) and image (**c**) is the
321 Jinfoshan karst area of southwestern China (photographed by Dr. Pingheng Yang, the Research Base
322 of Karst Eco-environments at Nanchuan in Chongqing, Ministry of Nature Resources, Southwest
323 University, China).

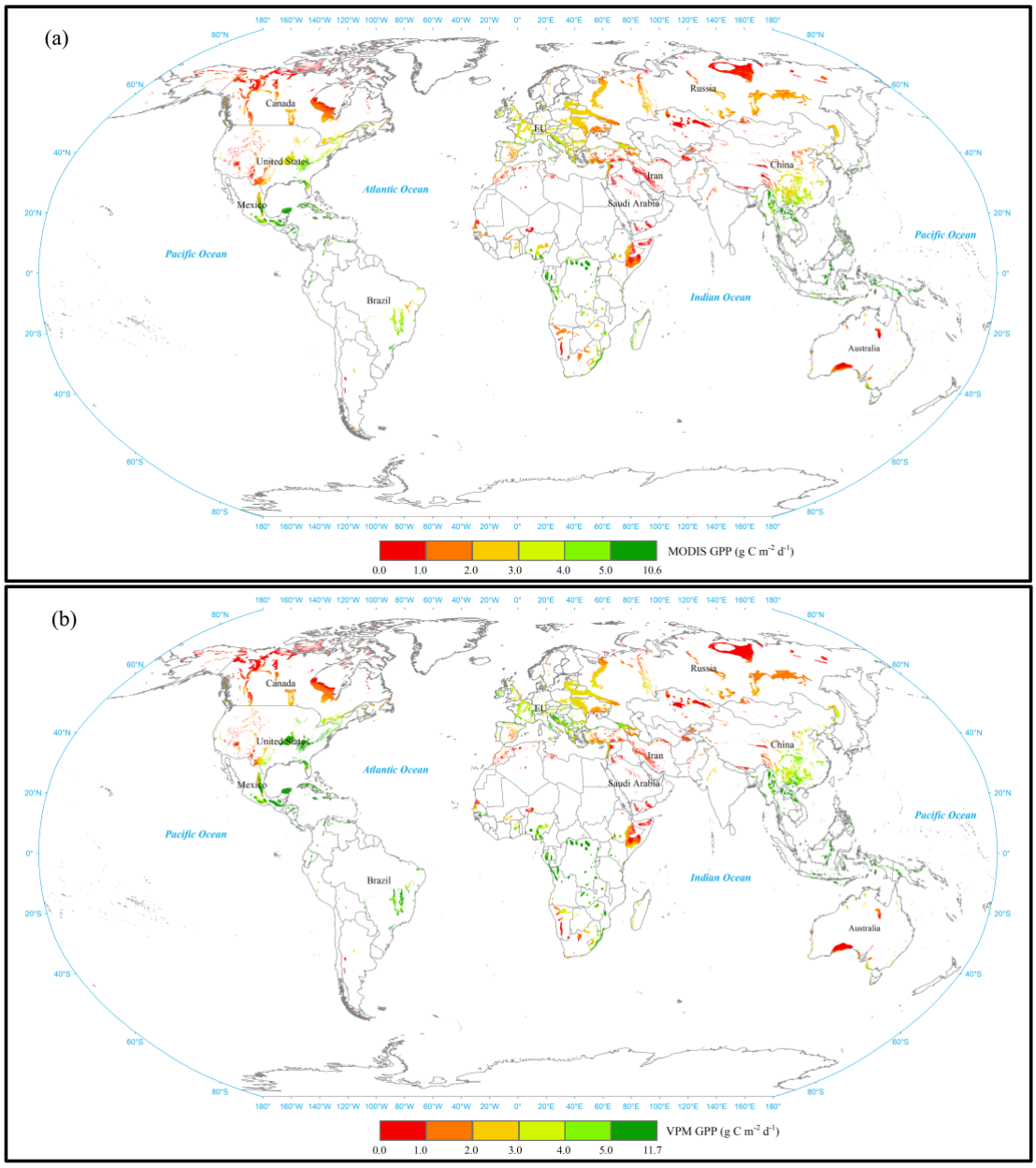


**Fig. 5** Magnitude and spatial patterns of multi-year mean MODIS GPP (a) and VPM GPP (b) across terrestrial ecosystems in global karst area.

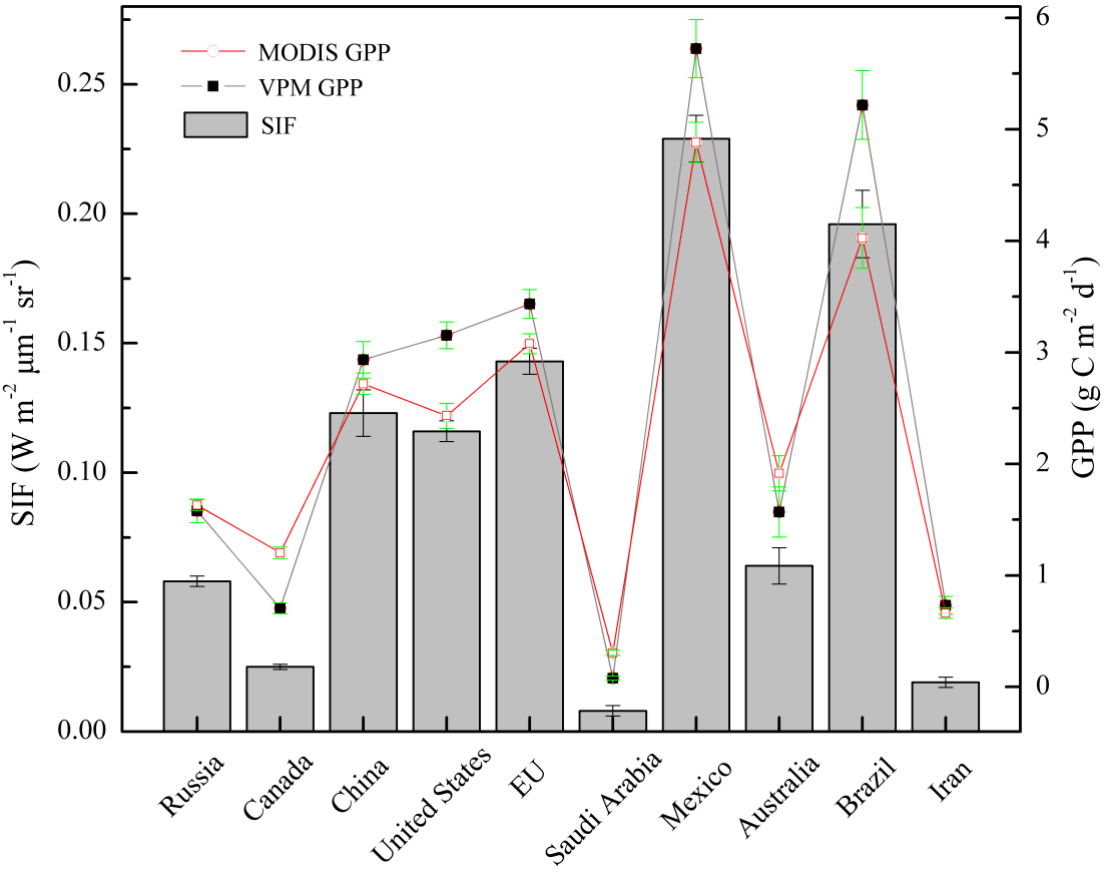


327 **Fig. 6** Multi-year mean SIF and GPP (MODIS and VPM) products in the top ten countries/region
328 with the largest karst areas. Error bars are ±1 standard error of the mean.

### *3.3. Contributions to the restoration of global karst ecosystems by country*

The absolute contributions to the global net changes were jointly determined by the karst area and magnitude of the changes. On the basis of the trend analysis in annual mean SIF across the karst regions between 2001 and 2016, the contribution rates of each country/region (the EU) to the restoration of ecologically-fragile karst areas are summarized in Fig. 7. Overall, the net increase mainly occurred in the northern hemisphere, while smaller increases and declines in SIF were more concentrated in the southern hemisphere. The top ten countries/region with the largest karst area contributed 78.04% of the global karst vegetation increase (Table 1). Most notably China, which has only 7.0% of the global karst area, accounted for 43.66% of the observed total net change. The EU (11.92%), Russia (11.82%) and Canada (6.78%) also made significant contributions. Although the USA has the fourth largest karst area, its contribution to global net change was only 2.03% (Table 1). Brazil was the only country amongst the top ten with a negative overall contribution (-1.85%).

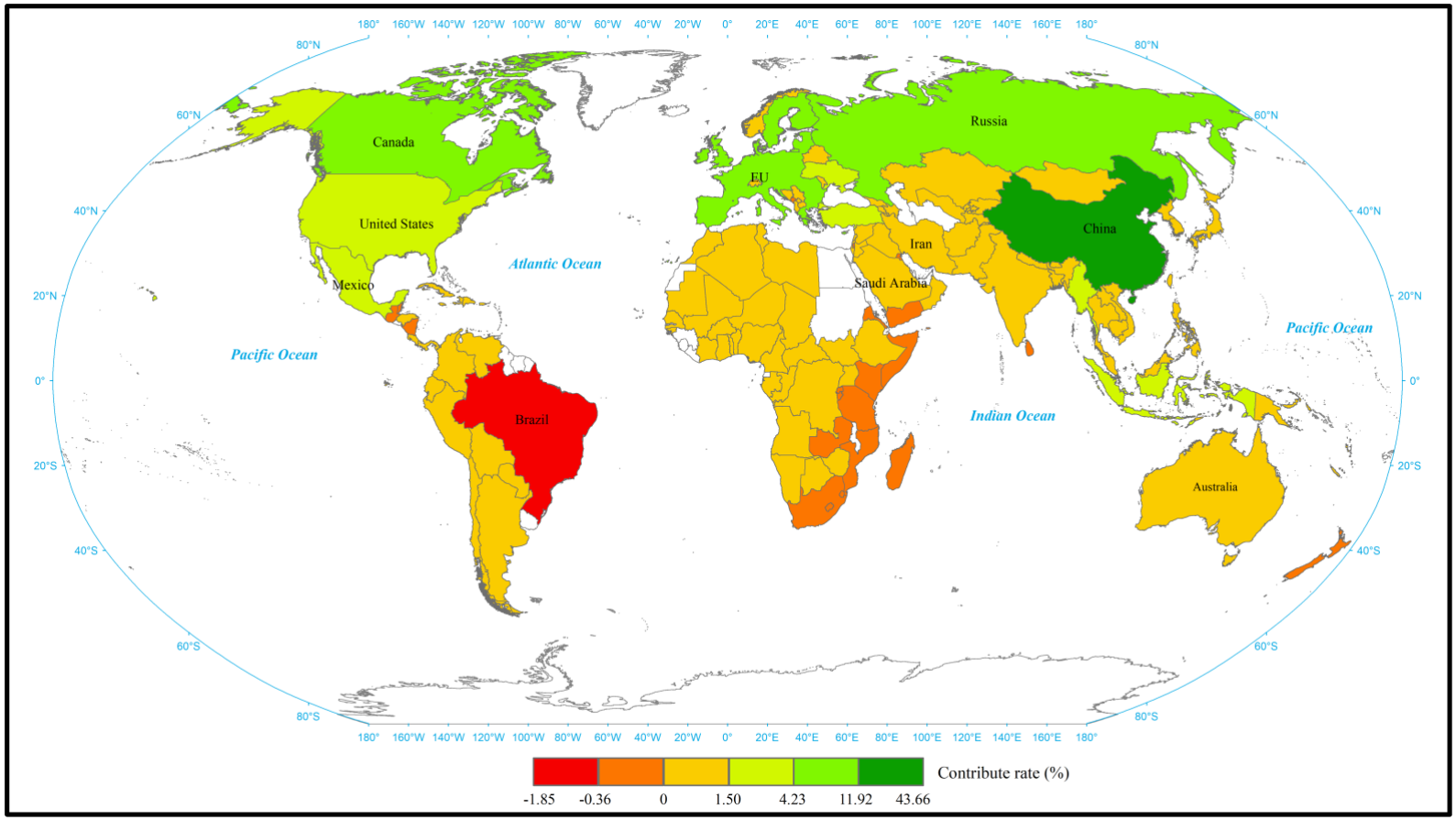


343

344 **Fig. 7** The contribution rates (%) of each country in restoring global karst ecosystem productivity. The countries of the European Union (EU) are considered together

345 given the large total karst area and relatively small size of some EU countries.

### *3.4. Environmental controls on vegetation restoration*

In order to explore the environmental controls on trends in vegetation dynamics across global karst area, we firstly performed a correlation analysis between time-series of SIF and meteorological data (Figs. 8 and 9). The analysis indicated that a large proportion of the changes in world's karst ecosystems were related to temperature and precipitation. More specifically, the area exhibiting significantly positive correlations was over twice as large as that associated with significantly negative correlations. Interestingly, temperature exerted predominantly positive effects in the northern hemisphere and negative effects in the southern hemisphere (e.g. Brazil, South Africa and Australia). Precipitation mainly exhibited negative correlations in high-latitude countries such as Russia and Canada. Partial correlations were also conducted to better understand the dominant environmental controls (Figs. S7 and S8). Results demonstrated spatial variability in the dominance of either temperature or precipitation upon SIF trends (Fig. 10). Approximately 17.26% of the total karst areas was strongly affected by precipitation ($p<0.05$); 10.70% of the area was obviously impacted by temperature ($p<0.05$); and only 3.66% of the area was jointly controlled by precipitation and temperature ($p<0.05$). A clear and consistent trend existed between the changes in precipitation and vegetation across a large portion of the global karst area. The karst area of eastern Canada was the largest spatially coherent region dominated by a positive relationship between temperature and vegetation productivity as indicated by SIF (Fig. 10, Fig. S8).

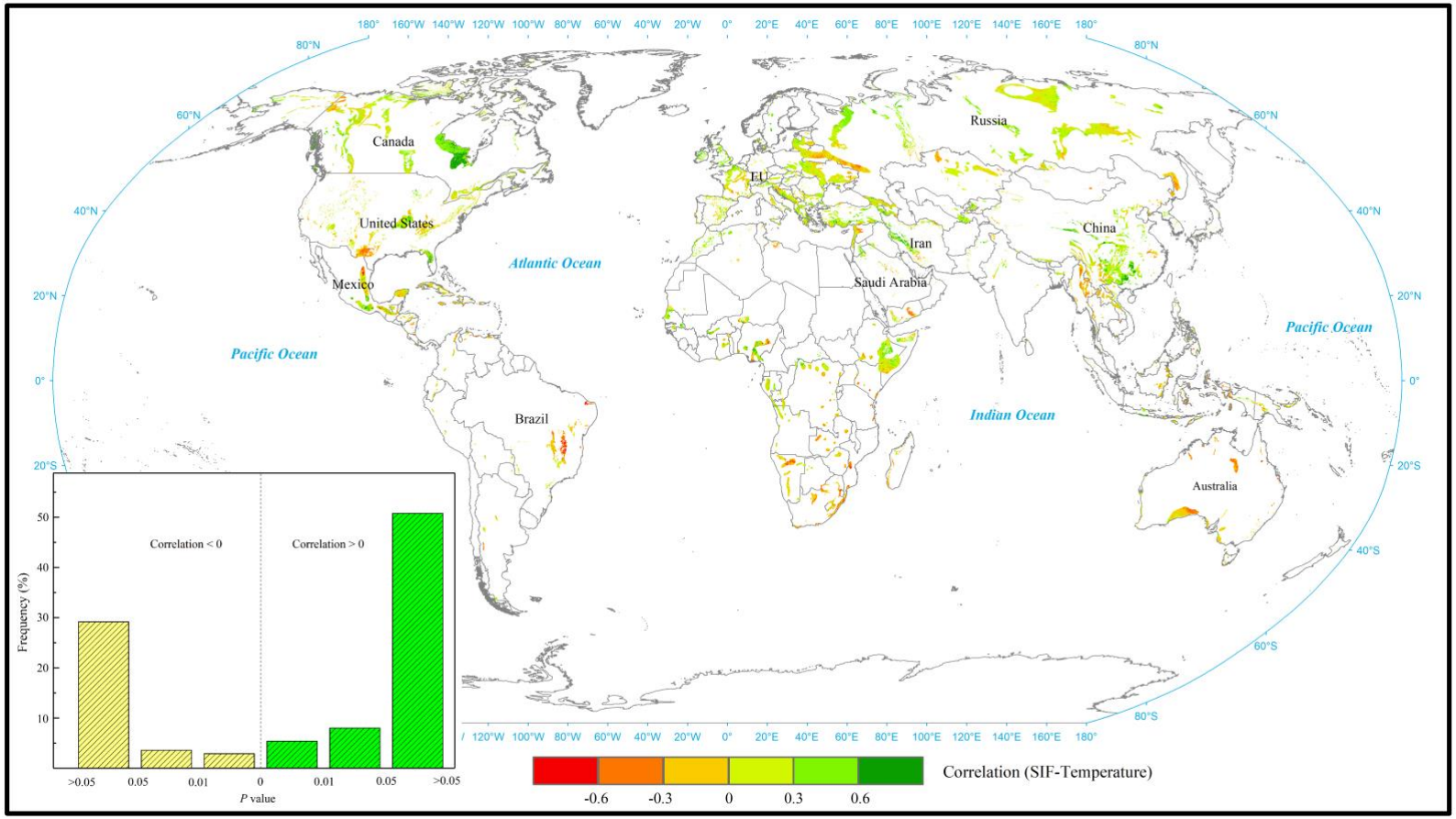


**Fig. 8** Spatial correlation analysis of annual mean SIF and temperature across terrestrial karst ecosystems during the period 2001–2016. The frequency distribution of the significance level (*p*-value) of the correlations is derived for each pixel.

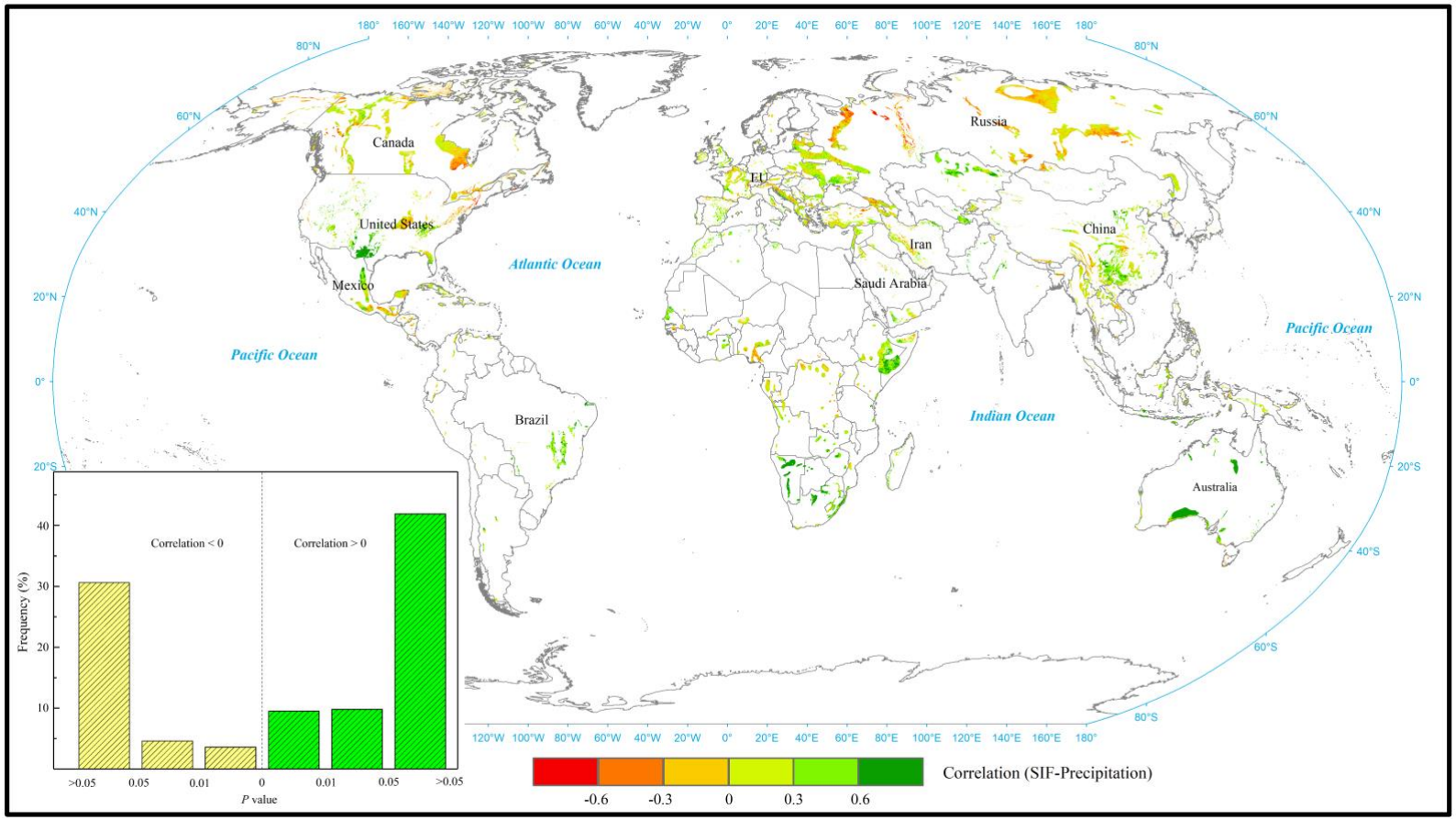


370

371 **Fig. 9** Spatial correlation analysis of annual mean SIF and precipitation across terrestrial karst ecosystems during the period 2001 – 2016. The frequency distribution

372 of the significance level (p-value) of the correlations is derived for each pixel.

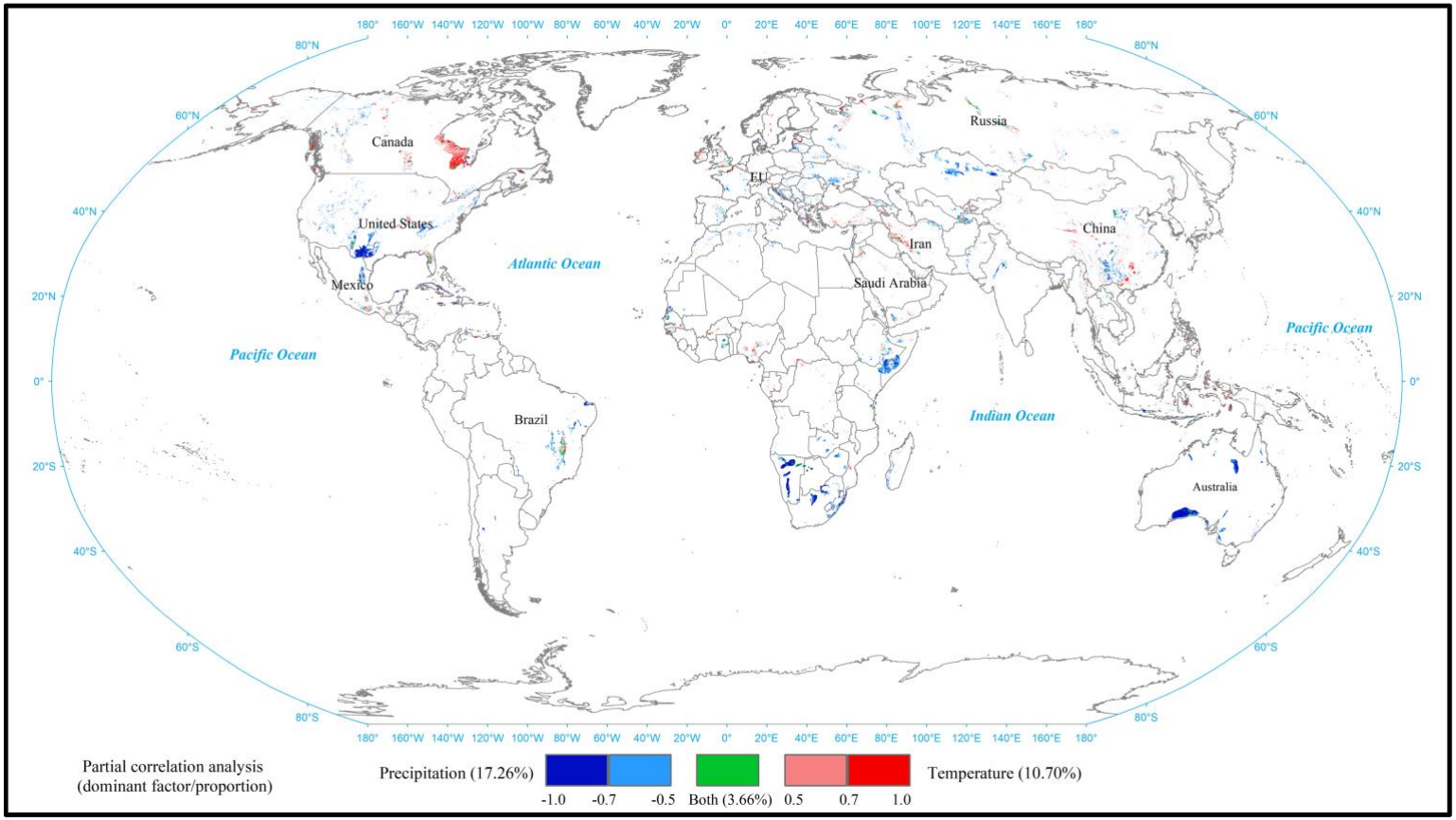


373

374 **Fig. 10** Dominant climatic factors (precipitation and temperature) controlling long-term trends in annual mean SIF across global karst ecosystems between 2001 and
375 2016. The partial correlation coefficients between SIF and temperature/precipitation that are significant at the 0.05 *p*-level are shown. The figure uses the positive and
376 negative values to describe the effects of temperature and precipitation, respectively. The proportions of karst area associated with dominant factors are indicated.

As reported above, the individual contribution of each country to the net increase in SIF for global karst ecosystems varied, ranging between 43.66% (China) and -1.85% (Brazil) for the top ten countries/region (the EU). The study further examined the effect of land cover changes due to human activities on karst areas in these two contrasting countries (Fig. 11). In China, forest, cropland and grassland together occupy over 85.0% of the total karst area (Fig. S9). With the implementation of a number of ecological restoration projects in China since 2001, large-area afforestation and conservation efforts improved the karst vegetation in approximately 45.10% of the regional change (Fig. 11a), which accounted for 36.93% of the increase in terrestrial SIF. In Brazil, forest, shrubland and cropland are the dominant land covers, occupying over 90% of the nation's karst areas (Fig. S10). Over the period 2001–2016, more than half of the land-cover changes were due to deforestation and this accounted for 64.71% of Brazil's decline in SIF for karst ecosystems (Fig. 11b).

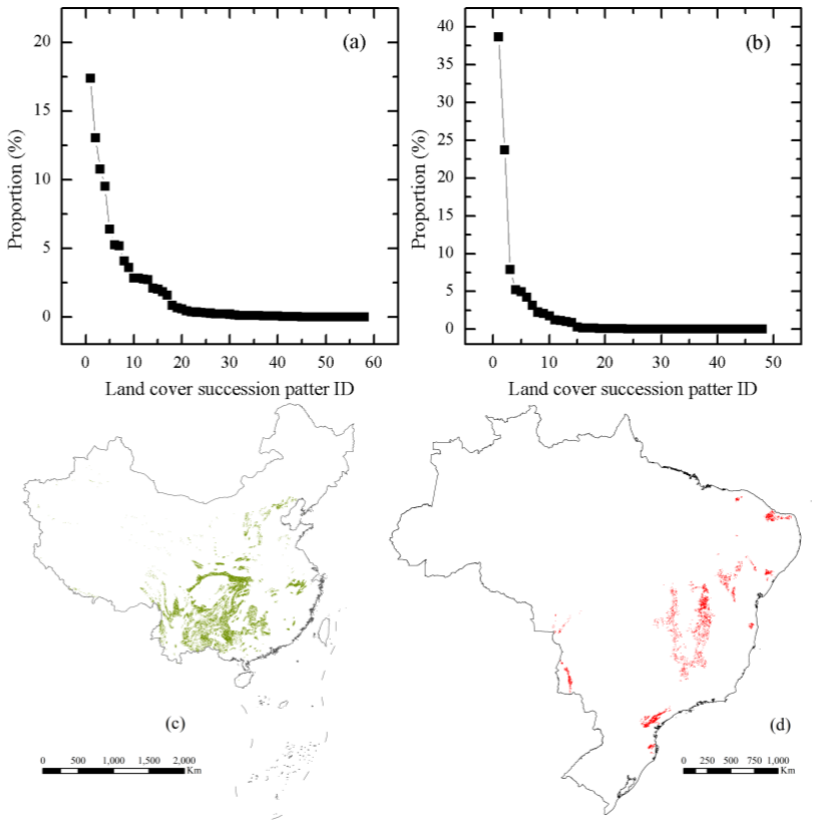


390

391 **Fig.11** Percentage of each land cover succession pattern amongst all land cover succession patterns
392 from 2001 to 2015 in the karst areas of China (a) and Brazil (b), respectively. (c) and (d) refer to
393 regions of grain-for-green programme in China and deforestation in Brazil, respectively.

## 394 4. Discussion and Conclusion

395 Karst rocky desertification has been reported in many regions including the
396 Mediterranean European, Dinaric Karst regions of the Balkan Peninsula, over a large
397 part of Southwest China, and most alarmingly, even in tropical rainforest areas underlain
398 by karstic geology such as in Haiti and Barbados (Jiang *et al.*, 2014). These changes
399 have tremendous environmental impacts with social-economic consequences at local to
400 national scales. It has been reported that severe soil erosion accompanied by vegetation
401 degradation within these ecologically-fragile areas have led to bedrock exposure
402 creating desert-like landscapes, reducing land productivity. As a result, economic

403 development has been constrained and poverty of local communities exacerbated (Yan
404 & Cai, 2015). Investigations of the dynamics of global karst ecosystems and the
405 associated driving forces are required in order to develop effective environmental
406 protection and sustainable development strategies.

407 In recent years, satellite-based observations and model simulations have revealed
408 the widespread greening of the Earth. Previous studies attributed the greening trend of
409 global vegetated area to the dominant role of climate change (Forzieri *et al.*, 2017;
410 Keenan *et al*., 2018) in addition to the effect of anthropogenic activities (Fan *et al*., 2019).
411 Nevertheless, climatic impacts on vegetation dynamics across different biomes and
412 climate zones are contrasting (Tang *et al*., 2017; Chen *et al*., 2019; Wang *et al*., 2021).
413 Forzieri et al. (2017) found that the increasing trend in leaf area index (LAI) contributed
414 to the warming of boreal zones through a reduction of surface albedo and to an
415 evaporation-driven cooling in arid regions. Our study has shown that vegetation changes
416 in most global karst area were affected by precipitation, and that only relatively small
417 area such as karst ecosystem in Canada, was dominantly influenced by temperature (Fig.
418 10). Climate warming was generally favorable for vegetation growth in global karst
419 areas except those in Brazil, South Africa and Australia (Fig. S8). Increasing
420 precipitation benefited vegetation restoration in most areas besides the northern high
421 latitudes (Fig. S9). In the karst region of eastern Canada, temperature declines resulted
422 in vegetation decrease, whereas increases in precipitation in Southwest China
423 significantly contributed to ecological restoration (Brandt *et al*., 2018). In the karst
424 regions of tropical Brazil, the apparent vegetation degradation was mainly driven by

425 climatic anomalies and human disturbance (Marengo *et al*., 2017; Servino *et al*., 2018).
426 Recently, model projections have suggested future increases in extreme climate events
427 such as droughts and heat waves around the world (Beniston *et al*., 2007; Zscheischler
428 *et al*., 2018), which will exert substantial pressure to the fragile karst ecosystems. The
429 sensitivity of ecosystems to climate perturbations can be partly reduced by appropriate
430 human management (Tong *et al*., 2018) but this clearly requires commitment from
431 governments.

432 Vegetation monitoring from traditional optical Earth observation (EO) datasets is
433 generally limited to the green canopy layer with less sensitivity to biomass (Tian *et al*.,
434 2016; Fan *et al*., 2019; Huang *et al*., 2021). As a result, the spatial pattern and trends of
435 productivity of global karst ecosystems remain poorly resolved. Whilst uncertainties
436 remain in the reconstructed global continuous SIF dataset, it provides direct and spatially
437 explicit information for quantitative monitoring of terrestrial photosynthesis and
438 ecosystem functions across multiple spatial and temporal scales. The spatial differences
439 in satellite-based ecosystem productivity across the globe are intrinsically determined
440 by the climate and vegetation-related characteristics. In the tropics and subtropics, owing
441 to favorable hydrothermal conditions, terrestrial ecosystems including forest, grassland
442 and shrubland are green almost all year round (Fig. S1). However, a large proportion of
443 vegetation in the mid- and high-latitudes is only active in summer and is then dormant
444 in winter. Yu *et al*. (2021) stated that ecologists should not only be able to monitor
445 dynamic changes in ecological processes, reveal mechanisms governing such processes,
446 and quantitatively assess ecosystem responses to human activities and climate changes,

447 but also provide accurate early warning of ecosystem changes.

448 Over the past few decades, intensive human pressure on land resulting from large
449 and rapidly growing human populations has been identified as a major threat to the
450 sustainable development of karst regions (Peng *et al.*, 2011), especially in rural areas
451 such as Southwest China (Yang *et al.*, 2017). Karst regions, lying in the upper reaches
452 of two of China's large rivers (the Yangtze and Pearl river), provide resources, in
453 particular water, for the two most economically-developed areas in China which are
454 located downstream in the rivers' delta regions (Bai *et al.*, 2013), while limited
455 conservation measures for these areas were in place during the 20$^{th}$ century. At the
456 beginning of the new millennium, the State Council of China released the 'Outline of the
457 10$^{th}$ Five-year Plan of National Economical and Social Development', which clearly
458 declared to fight against disastrous rocky desertification issues in southwestern China.
459 Subsequently, a series of key national ecological restoration projects including the
460 Natural Forest Protection Project, the Grain to Green Programme, the Karst Rocky
461 Desertification Comprehensive Control and Restoration Project and the River Shelter
462 Forest Project were launched to restore degraded karst and other ecosystems. The year
463 2001 is therefore an ideal starting point with which to compare changes in China's karst
464 environments and thereby to assess of the effects of these schemes. Our results indicate
465 that China contains one of the largest coherent karst regions and accounts for 43.66%
466 of the observed total net change in global SIF between 2001 and 2016 (Table 1, Fig. 7).
467 These findings corroborate other recent studies that have suggested that implementation
468 of the afforestation and reforestation projects during this period has significantly

increased vegetation growth and ecosystem carbon sequestration for mitigating global climate change (Lu *et al*., 2018; Tong *et al*., 2018). In addition, this study found that except China, the EU, Russia, Canada, the USA and several Southeast Asia countries also made positive contributions.

Within South America, karst landscapes cover 2% of the land area (370, 809 $km^2$), the majority of which is in Brazil and comprises woody savanna from open grasslands to forests. Despite a persistent and widespread increase in SIF for global karst ecosystems, this study found that approximately 19.43% of the karst area in Brazil was subject to serious vegetation degeneration over the period 2001–2016. As a result, Brazil makes a negative contribution to global greening of karstic environments (Fig. 7, Table 1). Currently, Brazil has become a global agricultural leader in the production of commodity raw crops such as soybean, sugarcane, cotton, and corn (Zalles *et al*., 2019). These crops often have short growth periods constraining their contribution to ecosystem productivity. Meanwhile, the carbon uptake by crops during their growth will be released to the atmosphere after much shorter periods compared to the forests that they often replace (West *et al*., 2010). Despite several strategic conservation measures to reverse deforestation (Nepstad *et al*., 2014), the rate of forest removal remains high in Brazil, endangering the long-term sustainability of the country and the global climate system (Schielein *et al*., 2018). Fig. 11 showed that the proportion of forest area declined over the study period. Artaxo (2019) reported that Amazonian forest, including in those areas underlain by karstic geology, is now suffering from losses at an accelerated rate through human-lit fires for agriculture. A recent study (Matricardi *et al*., 2020) also revealed that

491 long-term forest degradation even surpassed deforestation in the Brazilian Amazon.
492 Chen *et al*. (2019) reported the leading and impressive changes in agricultural
493 production in Brazil, but the greening from croplands is nearly offset by the browning
494 of forest. Besides, this study revealed that many countries in East Africa such as
495 Tanzania, Mozambique, Madagascar and South Africa are experiencing browning in the
496 past decades. Therefore, irrational land use and forest cutting could result in serious land
497 degradation, and the decrease of vegetation productivity. It is crucial for a global joint
498 action on karst environmental protection, otherwise gains in one area can be easily offset
499 by loss in other areas. These analyses have immediate implications for societal grand
500 challenges in relation to climate change mitigation as formulated by the UN Sustainable
501 Development Goals.

502 Our study found that these satellite-derived products were easy to characterize
503 spatial differences in vegetation productivity across global karst ecosystems (Figs. 1
504 and 2). However, contrasting performances were revealed when such products aimed
505 to capture interannual or long-term dynamics, just like Figs. 5 and 6 showed that these
506 remote sensing variables exhibited significantly different trends both globally and in
507 different countries. Compared with the MODIS GPP product, the SIF observations
508 indirectly confirmed the better performance of the VPM GPP results (Chen *et al*., 2019).
509 It can be ascribed to an improved light use efficiency parameter with the separate
510 treatment for $C_3$/$C_4$ photosynthesis pathways in the VPM model. Thus, the knowledge
511 derived from the global assessment herein can improve our understanding of both global
512 and regional ecosystem dynamics. Meanwhile, appropriate ecosystem management can

help to ensure regional ecological security and sustainable development. Nevertheless, it is necessary to take into account the country's own level of socio-economic development and the difficulty of restoring karst areas in the region. This forms an important foundation for a better management of karst ecosystems that include an effective mitigation of vegetation degradation.

## References


Artaxo, P. (2019). Working together for Amazonia. Science, 363(6425), 323.

Bai, X. Y., Wang, S. J., & Xiong, K. N. (2013). Assessing spatial-temporal evolution processes of karst rocky desertification land: indications for restoration strategies. Land Degradation & Development, 24(1), 47-56.

Beniston, M., Stephenson, D. B., Christensen, O. B., Ferro, C. A., Frei, C., Goyette, S., *et al*. (2007). Future extreme events in European climate: an exploration of regional climate model projections. Climatic Change, 81(1), 71-95.

Brandt, M., Yue, Y., Wigneron, J. P., Tong, X., Tian, F., Jepsen, M. R., *et al.* (2018). Satellite-observed major greening and biomass increase in south China karst during recent decade. Earth's Future, 6(7), 1017-1028.

Chen, C., Park, T., Wang, X., Piao, S., Xu, B., Chaturvedi, R. K., *et al*. (2019). China and India lead in greening of the world through land-use management. Nature Sustainability, 2(2), 122-129.

Chen, Y., Gu, H., Wang, M., Gu, Q., Ding, Z., Ma, M., *et al.* (2019). Contrasting performance of the remotely-derived GPP products over different climate zones across China. Remote Sensing, 11(16), 1855.

De Waele, J., Gutierrez, F., & Audra, P. (2015). Karst geomorphology: From hydrological functioning to palaeoenvironmental reconstructions. Part II. Geomorphology, 247, 1-1.

Fan, L., Wigneron, J. P., Ciais, P., Chave, J., Brandt, M., Fensholt, R., *et al.* (2019). Satellite-

observed pantropical carbon dynamics. Nature Plants, 5(9), 944-951.

Fensholt, R., Langanke, T., Rasmussen, K., Reenberg, A., Prince, S. D., Tucker, C., *et al*. (2012). Greenness in semi-arid areas across the globe 1981–2007—an Earth Observing Satellite based analysis of trends and drivers. Remote Sensing of Environment, 121, 144-158.

Ford, D., & Williams, P. D. (2013). Karst hydrogeology and geomorphology. John Wiley & Sons.

Forzieri, G., Alkama, R., Miralles, D. G., & Cescatti, A. (2017). Satellites reveal contrasting responses of regional climate to the widespread greening of Earth. Science, 356(6343), 1180-1184.

Areas, G. A. (2018). GADM database of Global Administrative Areas, version 3.6.

Gocic, M., & Trajkovic, S. (2013). Analysis of changes in meteorological variables using Mann-Kendall and Sen's slope estimator statistical tests in Serbia. Global and Planetary Change, 100, 172-182.

Grimm, N. B., Chapin III, F. S., Bierwagen, B., Gonzalez, P., Groffman, P. M., Luo, Y., *et al*. (2013). The impacts of climate change on ecosystem structure and function. Frontiers in Ecology and the Environment, 11(9), 474-482.

Guanter, L., Zhang, Y., Jung, M., Joiner, J., Voigt, M., Berry, J. A., *et al*. (2014). Global and time-resolved monitoring of crop photosynthesis with chlorophyll fluorescence. Proceedings of the National Academy of Sciences, 111(14), E1327-E1333.

Hiroko, B. & Rodell, M. (2016). GLDAS Noah Land Surface Model L4 Monthly 0.25 x 0.25 degree V2.1. NASA.

Huang, J., Ge, Z., Huang, Y., Tang, X., Shi, Z., Lai, P., *et al*. (2021). Climate change and ecological engineering jointly induced vegetation greening in global karst regions from 2001 to 2020. Plant and Soil, 1-20.

Jiang, Z., Lian, Y., & Qin, X. (2014). Rocky desertification in Southwest China: impacts, causes, and restoration. Earth-Science Reviews, 132, 1-12.

Ju, J., & Masek, J. G. (2016). The vegetation greenness trend in Canada and US Alaska from 1984–

563 2012 Landsat data. Remote Sensing of Environment, 176, 1-16.

564 Keenan, T. F., & Riley, W. J. (2018). Greening of the land surface in the world's cold regions
565 consistent with recent warming. Nature Climate Change, 8(9), 825-828.

566 Laffoon, M., Meier, A., & Groves, C. (2015). Potential Application of Hugelkultur to Increase Water
567 Holding Capacity of Karst Rocky Desertified Land.

568 Li, X., & Xiao, J. (2019). A global, 0.05-degree product of solar-induced chlorophyll fluorescence
569 derived from OCO-2, MODIS, and reanalysis data. Remote Sensing, 11(5), 517.

570 Li, X., Xiao, J., He, B., Altaf Arain, M., Beringer, J., Desai, A. R., *et al.* (2018). Solar-induced
571 chlorophyll fluorescence is strongly correlated with terrestrial photosynthesis for a wide variety
572 of biomes: First global analysis based on OCO-2 and flux tower observations. Global Change
573 Biology, 24(9), 3990-4008.

574 Lu, F., Hu, H., Sun, W., Zhu, J., Liu, G., Zhou, W., *et al*. (2018). Effects of national ecological
575 restoration projects on carbon sequestration in China from 2001 to 2010. Proceedings of the
576 National Academy of Sciences, 115(16), 4039-4044.

577 Magney, T. S., Bowling, D. R., Logan, B. A., Grossmann, K., Stutz, J., Blanken, P. D., *et al*. (2019).
578 Mechanistic evidence for tracking the seasonality of photosynthesis with solar-induced
579 fluorescence. Proceedings of the National Academy of Sciences, 116(24), 11640-11645.

580 Mao, J., Ribes, A., Yan, B., Shi, X., Thornton, P. E., Séférian, R., *et al*. (2016). Human-induced
581 greening of the northern extratropical land surface. Nature Climate Change, 6(10), 959-963.

582 Marengo, J. A., Torres, R. R., & Alves, L. M. (2017). Drought in Northeast Brazil—past, present,
583 and future. Theoretical and Applied Climatology, 129(3), 1189-1200.

584 Matricardi, E. A. T., Skole, D. L., Costa, O. B., Pedlowski, M. A., Samek, J. H., & Miguel, E. P.
585 (2020). Long-term forest degradation surpasses deforestation in the Brazilian Amazon. Science,
586 369(6509), 1378-1382.

587 Nepstad, D., McGrath, D., Stickler, C., Alencar, A., Azevedo, A., Swette, B., *et al*. (2014). Slowing
588 Amazon deforestation through public policy and interventions in beef and soy supply chains.

589 Science, 344(6188), 1118-1123.

590 Peng, J., Xu, Y., Cai, Y., & Xiao, H. (2011). Climatic and anthropogenic drivers of land use/cover
591 change in fragile karst areas of southwest China since the early 1970s: a case study on the
592 Maotiaohe watershed. Environmental Earth Sciences, 64(8), 2107-2118.

593 Piao, S., Yin, G., Tan, J., Cheng, L., Huang, M., Li, Y., *et al*. (2015). Detection and attribution of
594 vegetation greening trend in China over the last 30 years. Global Change Biology, 21(4), 1601-
595 1609.

596 Poulter, B., MacBean, N., Hartley, A., Khlystova, I., Arino, O., Betts, R., *et al*. (2015). Plant
597 functional type classification for earth system models: results from the European Space
598 Agency's Land Cover Climate Change Initiative. Geoscientific Model Development, 8(7),
599 2315-2328.

600 Schielein, J., & Börner, J. (2018). Recent transformations of land-use and land-cover dynamics
601 across different deforestation frontiers in the Brazilian Amazon. Land Use Policy, 76, 81-94.

602 Servino, R. N., de Oliveira Gomes, L. E., & Bernardino, A. F. (2018). Extreme weather impacts on
603 tropical mangrove forests in the Eastern Brazil Marine Ecoregion. Science of the Total
604 Environment, 628, 233-240.

605 Sun, Y., Frankenberg, C., Wood, J. D., Schimel, D. S., Jung, M., Guanter, L., *et al*. (2017). OCO-2
606 advances photosynthesis observation from space via solar-induced chlorophyll fluorescence.
607 Science, 358(6360).

608 Tang, X., Li, H., Ma, M., Yao, L., Peichl, M., Arain, A., *et al.* (2017). How do disturbances and
609 climate effects on carbon and water fluxes differ between multi-aged and even-aged coniferous
610 forests?. Science of the Total Environment, 599, 1583-1597.

611 Tang, X., Li, H., Desai, A. R., Nagy, Z., Luo, J., Kolb, T. E., *et al*. (2014). How is water-use
612 efficiency of terrestrial ecosystems distributed and changing on Earth?. Scientific Reports, 4(1),
613 1-11.

614 Tian, F., Brandt, M., Liu, Y. Y., Verger, A., Tagesson, T., Diouf, A. A., *et al*. (2016). Remote sensing

615 of vegetation dynamics in drylands: Evaluating vegetation optical depth (VOD) using AVHRR
616 NDVI and in situ green biomass data over West African Sahel. Remote Sensing of Environment,
617 177, 265-276.

618 Tong, X., Brandt, M., Yue, Y., Horion, S., Wang, K., De Keersmaecker, W., *et al*. (2018). Increased
619 vegetation growth and carbon stock in China karst via ecological engineering. Nature
620 Sustainability, 1(1), 44-50.

621 Walther, S., Voigt, M., Thum, T., Gonsamo, A., Zhang, Y., Köhler, P., *et al*. (2016). Satellite
622 chlorophyll fluorescence measurements reveal large-scale decoupling of photosynthesis and
623 greenness dynamics in boreal evergreen forests. Global Change Biology, 22(9), 2979-2996.

624 Wang, M., Ding, Z., Wu, C., Song, L., Ma, M., Yu, P., *et al*. (2021). Divergent responses of
625 ecosystem water-use efficiency to extreme seasonal droughts in Southwest China. Science of
626 The Total Environment, 760, 143427.

627 Wang, X., Xiao, J., Li, X., Cheng, G., Ma, M., Zhu, G., *et al*. (2019). No trends in spring and autumn
628 phenology during the global warming hiatus. Nature Communications, 10(1), 1-10.

629 West, P. C., Gibbs, H. K., Monfreda, C., Wagner, J., Barford, C. C., Carpenter, S. R., & Foley, J. A.
630 (2010). Trading carbon for food: Global comparison of carbon stocks vs. crop yields on
631 agricultural land. Proceedings of the National Academy of Sciences, 107(46), 19645-19648.

632 Wu, X., Xiao, X., Zhang, Y., He, W., Wolf, S., Chen, J., *et al*. (2018). Spatiotemporal consistency
633 of four gross primary production products and solar-induced chlorophyll fluorescence in
634 response to climate extremes across CONUS in 2012. Journal of Geophysical Research:
635 Biogeosciences, 123(10), 3140-3161.

636 Deng, Y., & Jiang, Z. C. (2011). Characteristic of rocky desertification and comprehensive
637 improving model in karst peak-cluster depression in Guohua, Guangxi, China. Procedia
638 Environmental Sciences, 10, 2449-2452.

639 Yan, X., & Cai, Y. L. (2015). Multi-scale anthropogenic driving forces of karst rocky desertification
640 in Southwest China. Land Degradation & Development, 26(2), 193-200.

641 Yang, H., Ma, M., Flower, R. J., Thompson, J. R., & Ge, W. (2017). Preserve Precambrian fossil
642 heritage from mining. Nature Ecology & Evolution, 1(8), 1048-1049.

643 Yang, Y., Xiao, P., Feng, X., & Li, H. (2017). Accuracy assessment of seven global land cover
644 datasets over China. ISPRS Journal of Photogrammetry and Remote Sensing, 125, 156-173.

645 Yu, G., Piao, S., Zhang, Y.,Liu, L.,Peng,J., Niu, S. (2021). Moving toward a new era of ecosystem
646 science. Geography & Sustainability, 2(3), 151-163.

647 Zalles, V., Hansen, M. C., Potapov, P. V., Stehman, S. V., Tyukavina, A., Pickens, A., *et al*. (2019).
648 Near doubling of Brazil's intensive row crop area since 2000. Proceedings of the National
649 Academy of Sciences, 116(2), 428-435.

650 Zhang, Y., Xiao, X., Wu, X., Zhou, S., Zhang, G., Qin, Y., & Dong, J. (2017). A global moderate
651 resolution dataset of gross primary production of vegetation for 2000–2016. Scientific Data,
652 4(1), 1-13.

653 Zhang, Y., Joiner, J., Alemohammad, S. H., Zhou, S., & Gentine, P. (2018). A global spatially
654 contiguous solar-induced fluorescence (CSIF) dataset using neural networks. Biogeosciences,
655 15(19), 5779-5800.

656 Zhang, Y., Zhang, Q., Liu, L., Zhang, Y., Wang, S., Ju, W., *et al*. (2021). ChinaSpec: a network for
657 long-term ground-based measurements of solar-induced fluorescence in China. Journal of
658 Geophysical Research: Biogeosciences, 126(3), e2020JG006042.

659 Zhao, M., Heinsch, F. A., Nemani, R. R., & Running, S. W. (2005). Improvements of the MODIS
660 terrestrial gross and net primary production global data set. Remote Sensing of Environment,
661 95(2), 164-176.

662 Zhu, Z., Piao, S., Myneni, R. B., Huang, M., Zeng, Z., Canadell, J. G., *et al*. (2016). Greening of
663 the Earth and its drivers. Nature Climate Change, 6(8), 791-795.

664 Zscheischler, J., Westra, S., Van Den Hurk, B. J., Seneviratne, S. I., Ward, P. J., Pitman, A., *et al*.
665 (2018). Future climate risk from compound events. Nature Climate Change, 8(6), 469-477.

666

## Acknowledgments

This study was jointly supported by the Special Project on National Science and Technology Basic Resources Investigation of China (Grant No. 2021FY100701) and the National Major Projects on High-Resolution Earth Observation System (Grant No. 21-Y20B01-9001-19/22). We would like to express our gratitude to all the scientists that have contributed to these multi-source datasets used in the study that includes the global OCO-2 SIF data set (GOSIF), VPM GPP and MODIS GPP products, the Climate Change Initiative Land Cover (CCI-LC) products (v2) and the meteorological data from the Global Land Assimilation System (GLDAS-2.1).

All data used in this study are publicly available. GOSIF data is available at http://data.globalecology.unh.edu/data/GOSIF_v2/. MODIS GPP is available at http://www.ntsg.umt.edu/project/mod17. VPM GPP can be downloaded from https://doi.org/10.6084/m9.figshare.c.3789814. CCI-LC products are available at http://maps.elie.ucl.ac.be/CCI/viewer/download.php. The meteorological data from the Global Land Assimilation System (GLDAS-2.1) can be downloaded via http://disc.sci.gsfc.nasa.gov/uui/datasets?keywords=GLDAS. The data on global country administrative areas (GADM V3.6) is available at https://gadm.org/data.html. The karst boundary is based on the World Map of Carbonate Rock Outcrops (V3.0) from the website https://www.fos.auckland.ac.nz/our_research/karst/.

## Author contributions

X.T. and C.W. designed the research. X.T. analyzed the data and wrote the paper. J.X.,

H.Y., Y.Z. and C.W. provided comments and suggestions. X.L., Z.D. and J.H. helped to process the data. M.M., P.Y., Q.G., H.Y. and J.R.T. provided valuable discussions and extensively revised the writing. All authors contributed ideas for analyses, comments and critiques.

## Additional information

**Supplementary Information** accompanies this paper with Figs. S1 to S9.

**Competing interests:** The authors declare no competing interests.